Contents

Chapter 1

Overview of Muography

Muography is an imaging technique that exploits the penetrating nature of cosmic muons to probe the internal structure of large and dense objects. These cosmic muons are produced as cosmic rays interact with the atmosphere of the Earth. Cosmic rays consist of a steady influx of high-energy particles originating from outer space. This phenomenon was first identified in 1912 by an Austrian physicist named Victor Hess. Hess conducted pioneering experiments by ascending to an impressive altitude of 5,300 meters in a hydrogen-filled balloon. At this elevation, he carefully measured the rate of ionisation in the atmosphere, discovering that it significantly increased compared to sea level. Notably, Hess found that this elevated rate of ionisation remained consistent, neither declining during the night nor during solar eclipses. His observations led him to conclude that the ionising radiation he detected was entering the Earth's atmosphere from above, a discovery he named cosmic rays [1]. These findings laid the groundwork for understanding cosmic radiation and its interactions with the atmosphere of the Earth.

In 1955, E.P. George made history by being the first to utilise cosmic-ray muons to inspect large structures. He measured the thickness of the rock situated above an ice tunnel in Australia [2]. In that same year, another application of cosmic-ray muons was introduced, proving that muons arriving horizontally along the Earth can probe the inner structure of a volcanic mountain [3]. Later, in 1970, a wider audience learned about the possibility of probing the content of large structures using cosmic muons due to Nobel Prize winner Luis W. Alvarez's investigation of Chephren's pyramid at Giza [4].

The use of muography has grown over the past decade. This rise in popularity is, for the most part, due to its broad range of applications across many different fields, including volcanology, archaeology, civil engineering, and nuclear waste monitoring, underground mapping, etc [5].

This chapter offers an overview of muon radiography. Section 1.1, delved into cosmic rays, while Section 1.2 provides a detailed look at the production and characteristics of cosmic muons. Section 1.3 outlines the fundamental principles of muon radiography as

they relate to volcanology. Finally, Section 1.4 highlights the various types of detectors commonly used in muography.

1.1 Physics of Cosmic rays

1.1.1 Primary cosmic-rays

The Earth is constantly bombarded by particles and nuclei from various astrophysical sources. These rays of particles are mainly composed of protons, with a smaller proportion of helium nuclei, while the rest includes heavier nuclei, extending up to iron. Such particles are also known as *primary cosmic-rays*, which are characterised by their high energy range from several hundreds of MeV to 10^{12} GeV. Figure 1.1 illustrates the broad energy spectrum of cosmic-rays reaching the Earth from space.
The flux of cosmic rays as a function of energy can be represented by a power law, expressed as $I(E) \propto E^{-\alpha}$. In this equation, I stands for the number of particles arriving per unit of time, area, and solid angle, while E represents the kinetic energy. The parameter α is referred to as the spectral index [7].

As Figure 1.1 shows, the spectrum deviates from the expected power law. At the lowest energies (< 30 GeV) up to $\mathcal{O}(10^6$ GeV), the so-called "knee", the spectrum follows a power law with spectral index $\alpha \sim 2.7$. For energies $\mathcal{O}(10^6$ GeV) to $\mathcal{O}(10^9$ GeV), the spectrum decreases with a spectral index $\alpha \sim 3.1$. The second spectral break, the second knee, is observed at an energy $\sim 10^9$ GeV, where the spectrum steepens ($\alpha \sim 3.3$). Measurements of the composition of CR in the region between the first and second knee indicate a shift in composition from predominantly protons to heavier elements. Near the second knee, the composition of CR consists mainly of iron[1] nuclei[8].
Finally, the spectrum reaches a third break, the ankle, at an energy of $\sim 10^{10}$ GeV. Cosmic-rays above 10^{10} GeV are called ultra-high energy cosmic rays and go on until a cut-off point is reached. The region between the second knee and the ankle is poorly understood. Presumably, the decrease refers to a transition between galactic and extragalactic sources [8]. Above the cut-off energy, the CR consists again mainly of protons. Protons at such high energies can interact with the photons of the cosmic microwave background (CMB) via the Δ resonance. This interaction is called the **GZK effect**. Heavier elements at these energies may also interact with the CMB, which causes them to photodisintegrate[2]. It is unknown whether the GZK effect is the only influence on the cut-off energy at the end of the spectrum. It is also possible that the limit with which a source can accelerate cosmic-rays can be a second influence. Detection of so-called GZK neutrinos would unambiguously prove the existence of the GZK effect. [9] [10]

[1] Star fusion can only produce elements up to iron. After a star's death, the produced elements are ejected from the core into the interstellar medium. Here they can be accelerated to become the CR, detected on Earth

[2] Phenomenon where the constituent nucleons are ripped apart [9].

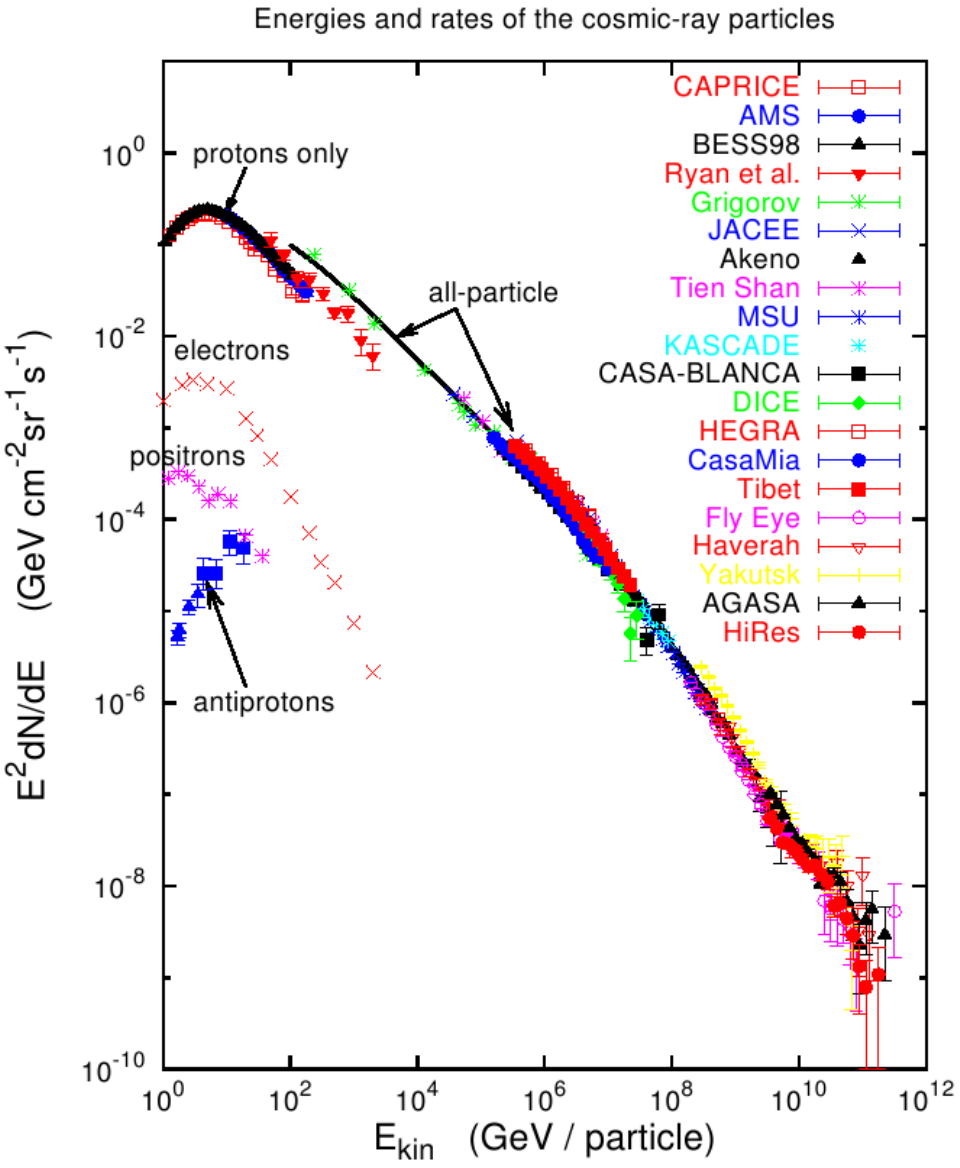

Figure 1.1: Measurements from different cosmic-ray experiments producing the cosmic-ray flux spectrum extending over 10 orders of magnitude [6].

1.1.2 Interactions in the Atmosphere and Secondary particles

Primary cosmic-ray particles reach the atmosphere of the Earth and interact with electrons and nuclei of atoms present in the air. The nuclear reactions caused by these interactions generate a cascade of processes leading to a shower of secondary particles, also called an Extended Air Shower (EAS). The air shower has three main components,

namely, a hadronic component, an electromagnetic component and a muonic component, illustrated in Figure 1.2.

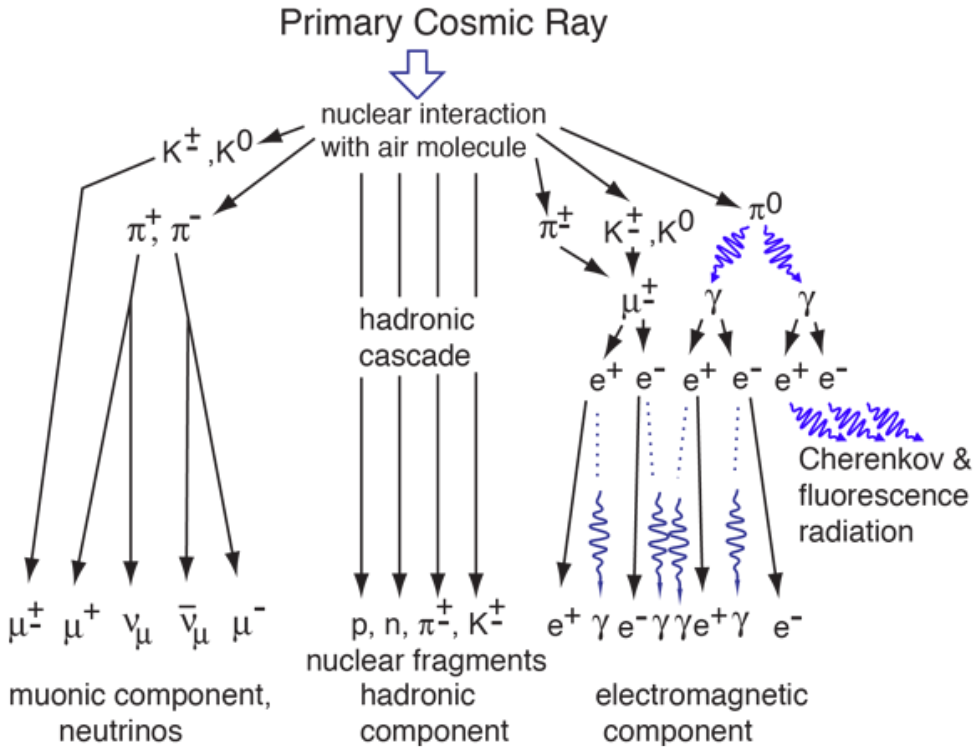

Figure 1.2: Illustration of the interaction between primary cosmic-rays with the atmosphere of the Earth, creating a cascade of secondary particles which is comprised of hadronic, electromagnetic and muonic components [11].

The initial interaction between cosmic rays and atmospheric particles generates a variety of secondary hadrons, with the primary ones being pions (π^+, π^-, π^0) and kaons (K^+, K^0). These secondary particles are essential in creating a hadronic cascade. As they continue to collide with nuclei in the atmosphere, they produce an even greater array of hadronic particles, including protons, neutrons, and additional types of mesons. This intricate network of interactions forms the foundational hadronic component of the particle shower. The neutral pions (π^0) decay almost instantaneously into two high-energy photons, which are critical for initiating the electromagnetic component of the shower. These photons subsequently interact with atmospheric atoms through processes such as pair production and bremsstrahlung, resulting in cascading emissions of electrons, positrons, and additional photons. The electromagnetic shower caused by these interactions is marked by the emission of Cherenkov radiation and fluorescence, phenomena that specialised observatories can effectively detect and analyse.

Among the secondary particles, charged pions (π^+ and $\pi-$) are particularly significant as they predominantly undergo a decay process into muons (μ^+, μ^-) and muon neutrinos (ν_μ^+, ν_μ^-). This decay typically occurs at lengths that allow the muons to travel far before being absorbed by matter, thanks to their relatively long lifetimes (2 μs) and weak interactions with surrounding particles. This characteristic enables many muons to reach ground-based detection instruments or traverse large thicknesses of rock, concrete, or other dense materials.

As the cascade propagates further through the atmosphere, the energy of the individual particles gradually decreases since the energy of the original particle initiating the shower gets more and more distributed across more secondary particles. The evolution of the cascade is governed by statistical models known as the cascade equations, which describe the decay and interaction probabilities. The calculation of these probabilities depends not only on the particle energy, altitude and zenith angle, θ, but also on the atmospheric depth, X (in gcm^{-2}) that a certain particle traverses. The atmospheric depth is defined as the integral of the height of the atmospheric density above the observational level, h, and for an isothermal atmospheric model, can be approximated as $X \approx e^{\frac{-h}{h_0}}$, where $h_0 \approx 8.4$ km is the atmospheric scale height.

Most secondary hadrons produced in the cascade are unstable and can decay as they travel through the atmosphere. The decay probability of a secondary particle depends on its mass, lifetime, momentum and the density of the medium. Because of energy losses and decays of the secondary particles, the total particle flux in the atmosphere increases with atmospheric depth until a maximum is reached at 100 gcm^{-2} corresponding to an altitude of approximately 20 km. After this point, the so-called Pfotzer maximum, the production of secondary particles maximises, and the particle flux dies down [7]. Moreover, the secondary cosmic-ray particles are categorised into two components based on their penetrating power. Firstly, the *soft component* is composed of electrons and low-energy muons since they get absorbed within a few centimetres of lead. Next, the *hard component* has a larger penetrating power, being able to reach sea-level, and contains high-energy hadrons and muons. Even though the contribution of both components varies with the altitude, the *hard* component, which is primarily made up of cosmic-ray muons, dominates at sea level, as shown in Figure 1.3.

A more thorough analysis of cosmic muons, their creation, interactions with matter, and the physical principles that make them perfect probes for muographic applications, like imaging the interior structure of Mount Vesuvius, is given in the section that follows.

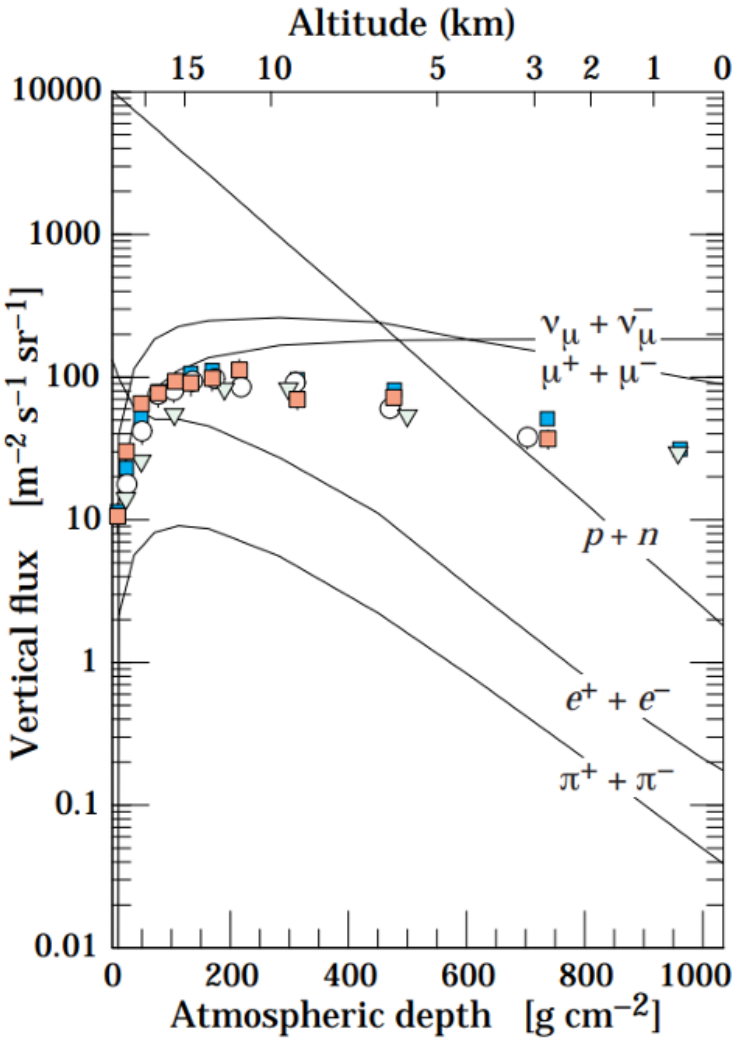

Figure 1.3: Vertical fluxes of cosmic rays in the atmosphere with energy greater than 1 GeV.

1.2 Cosmic Muons and Their Properties

1.2.1 Production and Characteristics

Muons are charged leptons with spin 1/2, charge -1 and a mass of 105.6 MeV/c^2, which is about ~ 200 times the mass of electrons. While muons can also be produced in particle accelerators, the muons used in muography applications originate from the atmosphere. Cosmic muons are produced as secondary particles when charged pions and kaons, most abundantly present in the EAS decay, via the following processes,

$$\pi \rightarrow \mu + \nu_\mu(\bar{\nu_\mu}) \tag{1.1}$$

$$K \rightarrow \mu + \nu_\mu(\bar{\nu_\mu}). \tag{1.2}$$

Muons are the most abundant secondary particles at sea level, as shown in Figure 1.3, despite their relatively short mean lifetime, τ, of $\sim 2.2\mu s$. Due to relativistic time dilation, the observed lifetime of cosmic muons is increased by the Lorentz factor $\gamma = 1/\sqrt{1-\beta^2} = \sqrt{1+(p/m_\mu)^2}$, where $\beta = v/c$ represents the relativistic speed and m_μ is the rest mass of a muon. For example, a muon with a momentum of 4 GeV experiences a Lorentz factor of about 20, increasing its lifetime enough such that it can travel around 24 km before decaying. Muons can easily reach sea level without decaying since their production mostly occurs at the Pfotzer maximum. [12] Furthermore, the primary sources of background in cosmic muon-based imaging are protons, electrons, and positrons, which likewise reach sea level without decaying. Because of their strong interaction with matter, they either dissipate or lose their energy more quickly than muons. Protons, in contrast to muons, are involved in nuclear interactions, and the energy loss from bremsstrahlung depends on $1/m^2$, meaning that muons lose about $40,000$ times less energy than electrons and positrons. The muon flux at sea level is therefore at least two orders of magnitude greater than any other charged particle and is predicted to be about 1 muon per second per cm^2, making it far higher than the overall background flux. [7]

Absorption of cosmic muons as they pass through a Volume of Interest (VOI) is the basis of many muography experiments. During these experiments, the free-sky muon flux is used to determine the attenuation caused by the VOI. Therefore, it is crucial that the flux can be precisely modelled to prevent biases and added uncertainties in the density extraction process. The Gaisser model describes the differential flux of muons at sea level as a function of their energy and the zenith angle [13]:

$$\frac{dN_\mu}{dE_\mu\, d\Omega} \approx 0.14 \cdot \frac{E_\mu^{-2.7}}{\mathrm{GeV} \cdot \mathrm{cm}^2 \cdot \mathrm{s} \cdot \mathrm{sr}} \left[\frac{1}{1 + \frac{1.1 E_\mu \cos\theta}{115\,\mathrm{GeV}}} + \frac{0.054}{1 + \frac{1.1 E_\mu \cos\theta}{850\,\mathrm{GeV}}} \right], \tag{1.3}$$

This module is most valid under these two conditions:

- $\theta < 70^\circ$, Earth's curvature does not influence muon paths
- muon decay is neglibible (E $> 100/\cos(\theta)$ GeV).

In muography experiments, where imaging of large volumes becomes important, the relevant muon trajectories are near-horizontal. This shortcoming of the model can be overcome by modifying the Gassier model such that larger zenith angles are included. The correction to the model includes a parameterisation of the zenith angle, taking the curvature of the Earth into account:

$$\cos\theta^* = \sqrt{\frac{(\cos\theta)^2 + P_1^2 + P_2(\cos\theta)^{P_3} + P_4(\cos\theta)^{P_5}}{1 + P_1^2 + P_2 + P_4}}$$

, where P_1, P_2, P_3, P_4 are P_5 are 0.102573, 0.06828, 0.958633, 0.0407253, and 0.817285, respectively [13]. An extra term is also added to the $E^{-2.7}$ factor, which becomes

negligible when the muon energy increases. The modified Gaisser model, now valid for larger zenith angles and lower energies, takes the following form:

$$\Phi_\mu(\theta, E) = 0.14 \cdot \left(\frac{E_\mu}{\text{GeV}} \left[1 + \frac{3.64\,\text{GeV}}{E_\mu (\cos\theta^*)^{1.29}} \right] \right)^{-2.7} \times \left[\frac{1}{1 + \frac{1.1 E_\mu \cos\theta^*}{115\,\text{GeV}}} + \frac{0.054}{1 + \frac{1.1 E_\mu \cos\theta^*}{850\,\text{GeV}}} \right] \tag{1.4}$$

1.2.2 Muon Energy loss in matter

When a charged particle travels through matter, it loses its energy and is deflected from its incident direction. These two effects are caused by inelastic collisions with atomic electrons in the traversed matter and elastic scattering from nuclei. Cosmic muons can penetrate large distances of the order $\mathcal{O}$(100m), with minimal energy loss and negligible electromagnetic cascade production. This makes them suitable for imaging large VOI, such as volcanoes. Furthermore, the energy loss and scattering bring valuable information about the traversed material.

The mean energy loss per unit path length for muons is given by

$$\frac{dE}{dx} = a(E) + b(E) \cdot E, \tag{1.5}$$

where the first term, $a(E)$, corresponds to the contribution of the ionisation and atomic excitation processes. For lower energies (< 100GeV, these processes can be described by the Bethe-Bloch relation:

$$-\frac{dE}{dX} = K z^2 \frac{Z}{A} \cdot \frac{1}{\beta^2} \left[\frac{1}{2} \ln \left(\frac{2 m_e c^2 \beta^2 \gamma^2 W_{\max}}{I^2} \right) - \beta^2 - \frac{\delta \beta\gamma}{2} \right], \tag{1.6}$$

where $K = 0.3071 MeV g/cm^2$ is a proportionality coëfficient, z the electric charge of the particle, Z/A the ratio between the atomic number and the atomic mass of the traversed medium, I is the mean excitation energy, m_e is the electron rest mass, W_{max} is the maximum energy that is transferred in a single collision and $\delta(\beta\gamma)$ represents a correction factor for the density.
The second term in Equation 1.6, $b(E)$, corresponds to the contribution of radiative processes like bremsstrahlung processes, pair production and nuclear interactions. This term slowly varies with energy and becomes asymptotically constant at higher muon energies, where its contribution becomes more significant. However, for many muography applications, the muons of interest generally have lower energies and as such, this contribution is minimal [14].

Practically in muography, the observed muon flux through an object measured by a muon detector is compared to the so-called "free-sky" flux. This comparison gives the probability for a muon to be absorbed by the traversed material along a certain line-of-sight, the so-called "muon transmission". This is the main idea behind absorption-based

muography. The muon transmission can be interpreted in terms of the opacity, defined as the integrated density along the line of sight and is usually expressed in units "meters water equivalent" (mwe): $1mwe = 100g/cm^2$. The average energy loss of a muon is approximately 0.2 GeV/mwe. [15]

1.2.3 Multiple Coulomb Scattering

Our current understanding of an atom was shaped in part by the Rutherford gold-foil experiment in 1911, which demonstrated how charged particles travelling through a medium are deflected from their path as a result of Coulomb interactions with the electric field around nuclei. The probability of the angular deflection $\Delta\theta$ for a single scattering follows Rutherford's scattering law,

$$P(\Delta\theta) \propto \frac{1}{\sin^4(\Delta\theta/2)}. \tag{1.7}$$

However, in many muography applications, muons undergo a large number of scatterings (> 20) and experience a minimal energy loss. Therefore, the net deflection angle as a function of the thickness can be treated statistically. According to the Central Limit Theorem, the actual distribution is approximately given by a Gaussian. 98% of the actual distribution can be accurately represented, with a zero mean value and standard deviation across a wide range of Z given by[16]:

$$\sigma_{\Delta\theta} = \frac{13.6 \text{ MeV}}{\beta cp} z \sqrt{\frac{x}{X_0}} \left[1 + 0.0038 \ln\left(\frac{xz^2}{X_0\beta^2}\right)\right], \tag{1.8}$$

where p is the muon momentum in MeV/c, z is the absolute electric muon charge (equal to 1), βc is the muon velocity, x is the total path length through the material, and X_0 is the radiation length of the material, empirically given by

$$X_0 \approx \frac{716.4 \text{ g/cm}^2 \cdot A}{Z(Z+1)\ln(286/\sqrt{Z})}, \tag{1.9}$$

where Z and A are the atomic number and mass of the material, respectively.
From Equations 1.8 and 1.9, it is clear that the Root Mean Square (RMS) of the scattering angle depend on the atomic number Z, making multiple Coulomb scattering sensitive to the composition of the traversed material. This principle forms the basis of scattering-based muography (SM). This type of imaging requires detecting muons before and after passing through an object to reconstruct its internal structure and identify areas with different atomic compositions. Therefore, SM requires installing detectors on both sides of the object to measure the diffusion angle. This requirement limits the size of the objects that can be imaged to a scale of approximately 1 to 10 meters.

In contrast, there are no restrictions on absorption-based imaging, allowing for the imaging of very large objects, such as volcanoes, using this technique. Therefore, the next section will give a more elaborate explanation of absorption muography.

1.3 Basic Principles of Muon Radiography

1.3.1 Absorption Muography

The absorption-based muography technique, AM, creates radiographic images by measuring the absorption rate, or transmission, as the muons pass through a volume of interest (VOI). This technique makes it possible to estimate the mean density along the path length of the traversed material for VOI, where the topographical information is known. In reverse, this technique can reveal possible density anomalies such as cavities, showing as an excess in flux, or high-density deposits revealed by a deficit of muon flux.

The concept of AM is similar to X-ray imaging, popularly used for medical purposes, but with some key differences. X-ray imaging uses tunable artificially produced X-rays, in contrast with the naturally occurring multi-directional muon flux for AM. In addition, muons can survive travelling through hundreds of meters of rock or other dense objects due to their hard penetrating nature, as opposed to X-rays, which can only survive a few meters. These properties of muons make them suitable for imaging large-scale structures like volcanoes or pyramids. A typical AM experiment measures the incoming muon flux as a function of the direction given by the zenith angle, θ and azimuthal angle, ϕ. The number of detected muons, N_μ, by the muon detector can be described by Equation 1.10, with the differential flux Φ_μ known in a certain angular direction.

$$N_\mu = t^\mu_{\text{acq}}\, \epsilon \int_{2\pi} S_{\text{eff}}(\Omega) \left[\int_{E_{\min}}^{\infty} \Phi_\mu(\Omega; E)\, dE \right] d\Omega, \tag{1.10}$$

where t^μ_{acq} represents the total data acquisition time, Ω is the solid angle with $d\Omega = sin(\theta) d\theta\phi$ the element of the solid angle, $S_{\text{eff}}(\Omega)$ is the effective surface-area of the telescope in the direction Ω, $\epsilon(E, \Omega)$ denotes the global efficiency.
The effective surface area $S_{\text{eff}}(\Omega)$ depends on the total sensitive area of the detector, S, and a geometrical factor $g(\Omega)$. $S_{\text{eff}}(\Omega)$ gives an estimation of the fraction of the total sensitive area involved in detecting the cosmic muons that come from Ω. The global efficiency is made up of three different quantities:

1 Trigger efficiency denotes how often the detector correctly identifies and records incoming muons;

2 Data-acquisition efficiency indicates the success of recording trigger events;

3 Analysis efficiency represents how well the real muon events survive data-analysis filters and cuts.

The number of muons that are observed depends on the traversed opacity, X, via the integration extreme in Equation 1.10, $E_{\min}$. This value represents the lower energy limit of the cosmic muons needed to create a signal in the detector after travelling through the VOI. It is defined as the sum of two different energy values, $E^{\text{rock}}_{\min}$, the minimum energy muons need to survive crossing the opacity X, and $E^{\text{det}}_{\min}$, the minimum energy

needed to be detected.

Besides the flux measurements from VOI, AM experiments also need measurements of calibration flux or *Free-sky* flux. Given the differential free-sky flux, the number of muons, N_{FS}, can again be described by Equation 1.10. In this case, $E_{\mathrm{min}} = E_{\mathrm{min}}^{\mathrm{det}}$ since the calibration measurements are done by taking data pointing the detector towards the open sky, i.e. $E_{\mathrm{min}}^{\mathrm{rock}} = 0$. These measurements must be done under the same conditions as the flux measurements from VOI. This ensures that the geometrical factor g and trigger efficiency ϵ_{trg} are equal for both modes. To evaluate the mass distribution of an object, the transmission, $T(\theta, \phi)$, defined as the effective ratio between the measured and the calibration flux, is used instead of the individual flux measurements. This ensures the cancellation of detector effects. The transmission is calculated as follows:

$$T_{\mathrm{mes}}(\theta, \phi) = C \cdot \frac{N_{\mathrm{VOI}}^{\mu}(\theta, \phi)}{N_{\mathrm{FS}}^{\mu}(\theta, \phi)}, \tag{1.11}$$

where C is a calculable constant that involves the data-acquisition times for both flux measurements and the efficiencies:

$$C = \frac{\epsilon_{\mathrm{DAC}}^{\mathrm{VOI}} \cdot \epsilon_{\mathrm{cuts}}^{\mathrm{VOI}}}{\epsilon_{\mathrm{DAC}}^{\mathrm{FS}} \cdot \epsilon_{\mathrm{cuts}}^{\mathrm{FS}}} \cdot \frac{t_{\mathrm{FS}}}{t_{\mathrm{VOI}}}. \tag{1.12}$$

To interpret the data in terms of material density, the expected transmission $T_{\mathrm{exp}}(\theta, \phi; \rho)$ must be computed. This depends on a muon flux model and the opacity of the material, often requiring Monte Carlo simulations, especially for complex geometries like volcanoes. The relative transmission, $R((\theta, \phi; \rho)$ is then defined as:

$$R(\theta, \phi; \rho) = \frac{T_{\mathrm{mes}}(\theta, \phi)}{T_{\mathrm{exp}}(\theta, \phi; \rho)}. \tag{1.13}$$

This ratio is expected to be 1 if cosmic muons cross a void or a region without any density anomalies. A cavity or a less dense region in the material is encountered for $R > 1$, while $R < 1$ suggests a denser region in the material.
Though AM primarily provides 2D projections, combining measurements from multiple viewpoints enables 3d density reconstructions. This involves solving an inverse problem by voxelizing the VOI and iteratively adjusting densities to fit the transmission data, using methods such as least-squares minimisation or Bayesian regularisation.

1.4 Detectors for Muon Radiography

In order to reconstruct trajectories and deduce the internal structure of a volume of interest (VOI), muon radiography depends on the detection of cosmic-ray muons with sufficient spatial and angular resolution. Numerous detector technologies have been created and used over time; each has advantages and disadvantages based on the application. The three primary types of detectors used in muography—nuclear emulsion detectors, scintillation detectors, and gaseous detectors—are summarised in this section.

1.4.1 Nuclear Emulsion Detectors

Nuclear emulsion detectors are one of the first detectors used as a particle tracking device. The principle of this detector type is similar to that of photography. The detector consists of a plastic or glass substrate coated with silver halide crystals mixed with gelatin. As a muon passes through, it produces ionisation, which sensitises the crystals along its path. After chemical development, this becomes visible as a track of silver grains. The main advantages include compactness, transportability, high spatial resolution ($\mathcal{O}$(1–10 μm)), and the fact that it works without any power supply. However, the detector loses efficiency when exposed to high temperatures, and because all events are reconstructed together on film, the data analysis can only be done at the end of the data-taking. In addition, there is no time information available, such that no dynamical monitoring of the structure can be done. A final drawback is that the track reconstruction is time-consuming and requires precise scanning using automated microscopes and sophisticated image processing software [16][17].

1.4.2 Scintillation Detectors

Scintillation detectors are used in various absorption muography applications. The main principle is that the detector responds by emitting light after interacting with the cosmic muons passing through. This light is collected, converted into electrons and amplified by photomultiplier tubes (PMTs) or, more recently, Silicon photomultipliers (SiPMs). Often, the scintillator bars are coupled with WLS fibres that absorb the primary light and re-emit photons at more suitable wavelengths for the photomultipliers. Typically, these detectors consist of two or more planes with two layers of orthogonal scintillator bars, making it possible to reconstruct the muon tracks in two independent projections.The resolution and sensitivity of the detectors are determined by the shape (rectangular, triangular, ...) and dimension. In recent years, SiPMs have become more commonly used due to their robustness, relatively low cost and applicability in harsh or logistically challenging environments. The main drawback for SiPMs is their temperature dependence: temperature variations affect the breakdown voltage, which in turn impacts gain, dark count rate, and reverse current [7] [15].

1.4.3 Gaseous Detectors

Gaseous detectors, such as drift chambers, resistive plate chambers (RPCs), and Micromegas, utilise ionisation produced by muons in a gas medium to detect their passage. The ionised electrons are then drifted under an electric field and collected on anode wires or pads, allowing for the reconstruction of the particle's trajectory.
These detectors are capable of covering large areas at a relatively low cost while providing good spatial resolution, typically ranging from hundreds of micrometres to a few millimetres. They are also designed to operate at high rates and are widely used in particle physics experiments, which has spurred their technical advancement and accessibility. In the field of muography, gaseous detectors are especially beneficial for

applications that demand high angular precision or for the development of large-area tracking systems. However, their complexity, along with the necessity for stable gas systems and high-voltage supplies, can pose challenges for field deployment when compared to scintillator-based systems[16] [15].

Bibliography

[1] Michael Walter. "Early Cosmic Ray Research with Balloons". In: *Nuclear Physics B - Proceedings Supplements* 239-240 (2013). Proceedings of the 9th workshop on Science with the New Generation of High Energy Gamma-ray Experiments: From high energy gamma sources to cosmic rays, one century after their discovery, pp. 11–18. ISSN: 0920-5632. DOI: https://doi.org/10.1016/j.nuclphysbps.2013.05.002. URL: https://www.sciencedirect.com/science/article/pii/S0920563213003691.

[2] E. P. George. "Cosmic Rays Measure Overburden of Tunnel". In: *Commonwealth Engineer* 42.12 (1955), pp. 455–457.

[3] K Nagamine et al. "Method of probing inner-structure of geophysical substance with the horizontal cosmic-ray muons and possible application to volcanic eruption prediction". In: *Nuclear Instruments and Methods in Physics Research Section A: Accelerators, Spectrometers, Detectors and Associated Equipment* 356.2 (1995), pp. 585–595. ISSN: 0168-9002. DOI: https://doi.org/10.1016/0168-9002(94)01169-9. URL: https://www.sciencedirect.com/science/article/pii/0168900294011699.

[4] Luis W. Alvarez et al. "Search for Hidden Chambers in the Pyramids". In: *Science* 167.3919 (1970), pp. 832–839. DOI: 10.1126/science.167.3919.832. eprint: https://www.science.org/doi/pdf/10.1126/science.167.3919.832. URL: https://www.science.org/doi/abs/10.1126/science.167.3919.832.

[5] Lorenzo Bonechi, Raffaello D'Alessandro, and Andrea Giammanco. "Atmospheric muons as an imaging tool". In: *Reviews in Physics* 5 (2020), p. 100038. ISSN: 2405-4283. DOI: https://doi.org/10.1016/j.revip.2020.100038. URL: https://www.sciencedirect.com/science/article/pii/S2405428320300010.

[6] A. M. Hillas. *Cosmic Rays: Recent Progress and some Current Questions*. 2006. arXiv: astro-ph/0607109 [astro-ph]. URL: https://arxiv.org/abs/astro-ph/0607109.

[7] Samip Basnet. "Muography : development of a portable detector and analysis of the MURAVES data". PhD thesis. Louvain U., 2024.

[8] Pablo Correa Camiroaga. "Merging Neutrino Astronomy with the Extreme Infrared Sky. A Search for Cosmic Neutrinos from Ultra-Luminous Infrared Galaxies with the IceCube Observatory". PhD thesis. Vrij Universiteit Brussel, Sciences Bio-Engineering Sciences Interuniversity Institute for High Energies, 2022.

[9] Thomas K. Gaisser, Ralph Engel, and Elisa Resconi. *Cosmic Rays and Particle Physics*. Cambridge University Press, June 2, 2016.

[10] Julia K. Becker. "High-energy neutrinos in the context of multimessenger astrophysics". In: *Physics Reports* 458.4-5 (Mar. 2008), pp. 173–246. DOI: 10.1016/j.physrep.2007.10.006. URL: https://doi.org/10.1016%2Fj.physrep.2007.10.006.

[11] *Cosmic rays*. URL: http://hyperphysics.phy-astr.gsu.edu/hbase/Astro/cosmic.html#c2.

[12] Gordon McIntosh et al. "The Regener-Pfotzer Maximum During a Total Solar Eclipse". In: *Journal of High Altitude Ballooning* 1 (Aug. 2021). DOI: 10.31274/jhab.13031.

[13] Mengyun Guan et al. *A parametrization of the cosmic-ray muon flux at sea-level*. 2015. arXiv: 1509.06176 [hep-ex]. URL: https://arxiv.org/abs/1509.06176.

[14] Francesco Riggi. "Interaction of Muons with Matter". In: *Messengers from the Cosmos: An Introduction to the Physics of Cosmic Rays in Its Historical Evolution*. Cham: Springer Nature Switzerland, 2023, pp. 241–247. ISBN: 978-3-031-24762-0. DOI: 10.1007/978-3-031-24762-0_13. URL: https://doi.org/10.1007/978-3-031-24762-0_13.

[15] S. Procureur. "Muon imaging: Principles, technologies and applications". In: *Nuclear Instruments and Methods in Physics Research Section A: Accelerators, Spectrometers, Detectors and Associated Equipment* 878 (2018). Radiation Imaging Techniques and Applications, pp. 169–179. ISSN: 0168-9002. DOI: https://doi.org/10.1016/j.nima.2017.08.004. URL: https://www.sciencedirect.com/science/article/pii/S0168900217308495.

[16] G. Bonomi et al. "Applications of cosmic-ray muons". In: *Progress in Particle and Nuclear Physics* 112 (2020), p. 103768. ISSN: 0146-6410. DOI: https://doi.org/10.1016/j.ppnp.2020.103768. URL: https://www.sciencedirect.com/science/article/pii/S0146641020300156.

[17] M. D'Errico et al. *The MURAVES experiment: study of the Vesuvius Great Cone with Muon Radiography*. 2022. arXiv: 2202.12000 [physics.ins-det]. URL: https://arxiv.org/abs/2202.12000.